The International Journal of Advanced Manufacturing Technology (2024) 132:835–851
https://doi.org/10.1007/s00170-024-13437-7

ORIGINAL ARTICLE

Analysis of the causes determining dimensional and geometrical errors in 316L and 17-4PH stainless steel parts fabricated by metal binder jetting

Marco Zago[1] · **Nora Lecis**[2] · **Marco Mariani**[2] · **Ilaria Cristofolini**[1]

Received: 29 November 2023 / Accepted: 11 March 2024 / Published online: 16 March 2024

Abstract
This work aims at investigating the causes affecting the dimensional and geometrical accuracy of holes in metal binder jetting stainless steel parts. Parallelepiped samples with a through hole were produced using AISI 316L and 17-4PH powders, differing for diameter (3, 4, 5 mm), and position of the axes with respect to the building plane (6, 9, 12 mm distance). Dimensions and geometrical characteristics were measured at green and sintered state by a coordinate measuring machine, determining the dimensional change and the geometrical characteristics. As expected, the shrinkage of linear dimensions is anisotropic; moreover, change in volume and sintered density are significantly affected by the position in the printing chamber. Higher shrinkage was measured along building direction (Z) – 18.5 ÷ 19.5%, than in the building plane – 16.5 ÷ 17.5%, and slightly higher shrinkage – 0.5 ÷ 0.8% was measured along powder spreading direction (X) than binder injection direction (Y). A variation up to 3% in relative density of sintered parts depending on the position in the building plane was observed in 316L. The dimensional change of diameters generally confirmed the shrinkage predicted by the model previously developed—difference between real and expected dimensional changes lower than 3%, except for three geometries (4 ÷ 6%). The cylindricity form error of sintered parts was strongly underestimated by the prediction model (up to 0.15 mm), but underestimation was considerably reduced (generally lower than 0.05 mm) adding the cylindricity form error due to printing. Dimensional and geometrical accuracy of holes are strongly affected by shape distortion of the parallelepiped geometry, in turn due to layer shifting and inhomogeneous green density during printing, and to the effect of frictional forces with trays during sintering. Gravity load effect was also observed on the holes closest to the building plane. Future work will improve the reliability of the prediction model implementing the results of the present work.

Keywords Additive manufacturing · Metal binder jetting · Shrinkage on sintering · Dimensional and geometrical accuracy and precision

1 Introduction

Binder jetting (BJ) is an additive manufacturing (AM) technique with strong potential for manufacturing of small and medium batches. With respect to other AM processes, BJ building rate is higher than building rate of both material extrusion processes and powder-based techniques, as Laser Powder Bed Fusion (L-PBF) and Direct Energy Deposition (DED). Moreover, the printing operation does not require vacuum or inert gas atmosphere in most cases, neither support structures in the powder bed or high energy source [1]. The build-up process occurs at room temperature, so that residual stresses, which can lead to part cracking or failure, do not represent an issue [2, 3]. The competitiveness is emphasized by the possibility of using different metal feedstocks [2, 3]. The interest in metal binder jetting (MBJ) is rapidly growing within research community and companies.

Nevertheless, controlling the dimensional and geometrical accuracy and precision of final products still represents major issue to be addressed, being size and shape determined by the different operations involved in BJ process—printing, curing, de-powdering, debinding, and sintering.

✉ Ilaria Cristofolini
ilaria.cristofolini@unitn.it

[1] Department of Industrial Engineering, University of Trento, Via Sommarive 9, 38123 Trento, Italy

[2] Department of Mechanical Engineering, Politecnico Di Milano, Via Privata La Masa 1, 20156 Milano, Italy

The 3D CAD file is converted to a machine-readable format (STL, AMF, STEP), which is imported in the printing software. The main process parameters, layer thickness and binder saturation among them, are set up by the operator. A blade or roller determines height and homogeneity of powder layers, while the liquid binder injected by the printhead defines the section of the product, previously computed by the discretization algorithm. By repeating powder spreading and binder injection, the part is built up. The part is removed from the printing box after curing (70 ÷ 200 °C), which enhances binder cross-linking and increases the strength of the green part [4]. Manual or automatic de-powdering allows removing any extra-powder, prior to debinding and sintering. Debinding consists in a chemical and/or thermal treatment aimed at removing the organic binder agent, while sintering at high temperature activates the diffusion mechanisms, which strongly bond the powders and reduce porosity, determining the final structure and microstructure.

The influence of materials characteristics and process conditions on the dimensional and geometrical precision has been widely investigated in recent studies, aiming at improving the quality of BJ parts [5]. Particle size distribution (PSD) strongly affects both packing and sintered density, and in turn variations in volume and dimensional changes. As reported by German et al., an optimum mixture of bimodal particles can improve the packing density and final sintered density, also reducing the sintering shrinkage [6], as experimentally verified in recent work using MBJ feedstocks [7, 8]. Green density is also affected by process parameters; decreasing layer thickness green density increases [9, 10], and proper binder saturation interval has to be identified to control densification and resulting geometrical characteristics [11–14]. The influence of binder distribution on densification of Al during sintering has also been studied by transmission synchrotron X-ray imaging in [15, 16], highlighting the need for both developing alternative binders, and properly developing binder deposition patterns. The role of particle size on densification of Ti6Al4V was investigated in [17], considering binder-induced powder aggregation. Build orientation [18, 19] and position in the building plane [20] also play significant role in determining geometrical precision. Lee et al. proposed a model for particle spreading based on discrete elements, highlighting that high rake velocity can determine particle segregation; bigger particles tend to segregate in front of the rake and PSD shifts towards finer region [21].

Sintering conditions, as isothermal sintering temperature, holding time, and sintering atmosphere, determine the final densification, and consequently the volumetric shrinkage [22, 23]. The shrinkage is anisotropic [24], and, depending on the shape, distortion on sintering may also occur, detrimentally affecting the geometrical characteristics [25]. Severe deformation of cantilever beams and overhanging structures caused by the gravity-induced load was numerically simulated by a viscous-plastic material constitutive model, and experimentally validated [26, 27]. Shape distortion can also derive from inhomogeneous green density; shape distortion of rectangular samples with local variation of green density was numerically modelled in [28]. Stevens et al. observed density variation as a function of the sample geometry, ascribing the phenomenon to the interaction between binder and powder [30]. The frictional force acting on the part surface in contact with the support plate can also determine inhomogeneous deformation on sintering, as simulated by FEM in [30].

From designer's perspective, the anisotropic dimensional change and any shape deformation on sintering have to be compensated, in order to control the dimensional and geometrical accuracy and precision. Process conditions for optimizing densification and obtaining linear scaling factors, to be applied to the green product, have been investigated in [22, 32]. Models describing the shape deformation, along with proposals for compensation, are presented in [25, 33–35].

Considering specific geometrical characteristics, the influence of the printing operation on flatness and cylindricity form errors has been studied. Arni and Gupta proposed an analytical equation for assessing flatness form error caused by the staircase effect of layer-by-layer manufacturing [36]. Similarly, Paul and Anand developed a model for estimating cylindricity form error [18]. Islam and Sacks measured the cylindricity form error of concentric cylinders, concluding that deviation could be ascribed to the interaction between layers during the printing process [37]. Ollison and Berisso observed that cylindricity form error in green parts is scarcely influenced by diameter, while the axis inclination with respect to the building orientation is more significant [38]. Cylinder orientation has also been investigated by Dahmen et al., reporting that inclination angle has lower influence on the cylindricity form error in MBJ parts than in parts fabricated by L-PBF process [39].

Interesting models are proposed in the literature for describing shrinkage and distortion of MBJ parts [26–28, 34, 35]; however, the geometrical characteristics are not specifically considered. On the other hand, papers specifically dealing with geometrical characteristics estimation [36, 18, 37–39] are less focused on the phenomena occurring during sintering, which determine shrinkage/deformation. The present work is aimed both at studying the phenomena responsible for anisotropic shrinkage in MBJ parts and at developing a model for predicting anisotropic shrinkage on sintering of BJ stainless steel parts, to be used as a tool for designers. The dimensional and geometrical variations are derived experimentally, and are the starting point of the procedure. The geometry of parts is carefully reconstructed through the features describing the boundary of samples,

measured in the green and sintered state by a coordinate measuring machine (CMM), thus deriving data which precisely describe the anisotropic shrinkage.

The dimensional and geometrical accuracy of four holes having different inclination with respect to the building plane (0°, 30°, 45°, 60°, and 90°) were investigated in [40]. Moreover, an analytical model was validated for predicting hole shrinkage and circularity form error deriving from the anisotropic shrinkage on sintering. An overall good agreement between empirical data and model prevision was observed, except for the smallest holes, whose shrinkage was significantly underestimated. The deviation was attributed to the combined effect of the gravity load of the mass of powders on the circular section, and to the viscous-plastic behavior of the material [41].

On the basis of the above studies, this paper aims at investigating in depth the influence of the different phenomena occurring during the whole MBJ process on the dimensional and geometrical accuracy of MBJ parts. Parallelepiped samples were fabricated using AISI 316L and 17-4PH stainless steel powders, characterized by a through hole with axis parallel to the building plane, differing for diameter (3, 4, 5 mm), and distance of the axis from the building plane (6, 9, 12 mm). Samples were measured by CMM before and after sintering for assessing the actual dimensional change and the variation of geometry. The anisotropic dimensional change of linear dimensions was related to the printing conditions and the position in the building chamber; the diameter shrinkage and the cylindricity form error were compared to the data predicted by the analytical model developed in a previous work [40]. The observed deviation was discussed and related to the phenomena occurring in the different steps of the process. In this way, it was possible to highlight the phenomena determining the shrinkage/shape deformation of the holes, distinguished by their size/position, also comparing two different materials. To the author's knowledge, this kind of investigation was not performed yet.

2 Materials and methods

2.1 Geometry of parts

This work aims at assessing the factors determining the dimensional and geometrical accuracy and precision of holes in MBJ products, as affected by size and position. Figure 1 shows the geometry of the investigated parts, parallelepiped samples with a through hole, whose axis is parallel to the building plane.

Referring to Fig. 1, nine geometries were defined, having a base of 13 mm × 13 mm (LX × LY) and a height of 18 mm (LZ); three different hole diameters (ϕ) were considered (3, 4, and 5 mm). The position of hole axis with respect to the building plane (Lϕ) was set up at 6, 9, and 12 mm distance, so that holes are equally spaced along the sample height. Table 1 reports the nominal dimensions of the holes and the identification codes used for distinguishing the samples on the basis of diameter (ϕ3, ϕ4, ϕ5) and position (L06, L09, L12).

CAD files were converted into STL format for the printing set-up. Three replicates each for the nine geometries were printed in a single batch. Numbers 1, 2, and 3 were marked on each replicate to identify the samples after de-powdering and sintering operations. The replicates were randomly distributed in the printing chamber in order to minimize any influence of the building location, highlighted by Vitolo et al. [20]. According to the reference system in Fig. 1:

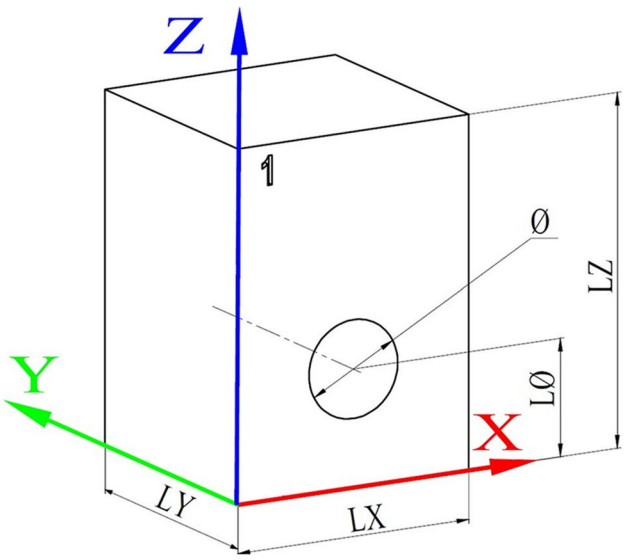

Fig. 1 Geometry and dimensions IDs of samples investigated

Table 1 Nominal dimensions of the geometries investigated

Geometry	Nominal dimensions	
	ϕ [mm]	$L\phi$ [mm]
ϕ3-L06	3	6
ϕ3-L09	3	9
ϕ3-L12	3	12
ϕ4-L06	4	6
ϕ4-L09	4	9
ϕ4-L12	4	12
ϕ5-L06	5	6
ϕ5-L09	5	9
ϕ5-L12	5	12

- X axis corresponds to the powder spreading and the movement of the roller;
- Y axis corresponds to the movement of the printhead;
- Z axis corresponds to the building direction.

For each sample, the hole axis is aligned parallel to the printhead movement direction (Y axis), which is the orientation allowing the better precision according to recent studies on slot features differently oriented in the building plane [42].

2.2 Materials and equipment

Samples were produced by an ExOne Innovent + 3D system using AISI 316L and 17-4PH stainless steel powders provided by Sandvik AB (Sweden). The declared particle size distribution of both 316L and 17-4PH powders features D90 < 22 µm. An aqueous-based binder was adopted, containing ethylene glycol monobutylether (EGBE), isopropanol (IPA), and ethylene glycol (EG), according to ExOne supplier. The main printing parameters are listed in Table 2; values were defined according to the previous investigation described in [43]. Aiming at minimizing the influence of noise factors, samples were produced in the same batch, using materials provided in a single supply.

After printing, the building box was carefully moved to the curing oven, for 6 h thermal treatment at 180 °C. Samples were then safely de-powdered and handled for the next measurements at the green state.

The dimensional and geometrical characteristics were measured by a coordinate measuring machine (CMM) Global DEA equipped with a Renishaw SP600 indexable head, which can guarantee a maximum permissible error of 1.5 + L/333 µm, in accordance with ISO 10360–2 [44]. After measurement, green samples of both materials were debinded at 470 °C for 4 h in Argon atmosphere and later at 650 °C for 1 h in vacuum, then sintered in a batch furnace. The isothermal sintering temperature was reached with a heating ramp of 5 °C/min; 316L samples were sintered at 1360 °C for 1 h, and 17-4PH samples at 1330 °C for 1 h. Samples were cooled down at an initial rate of 500 °C/min. The whole sintering cycle was carried out in vacuum atmosphere (10^{-1} mbar).

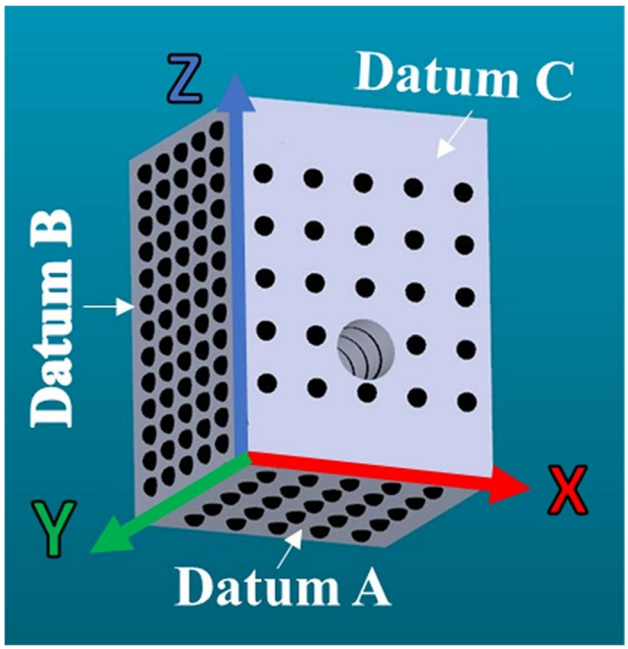

Fig. 2 Example of the measured points – geometry ϕ3-L06

2.3 Measurement procedure

The measurement procedure firstly established the datum reference frame on the sample (DRF), and samples were constrained accordingly, by a specific clamping system aimed at limiting as much as possible the hidden areas. According to the reference system shown in Fig. 1, four points are measured manually on the plane XY, to be used for reconstructing the primary datum plane (Datum A) by best-fit least squares method. Datum A fixed the origin and direction of Z axis (orthogonal to A). Four points were then measured on the plane YZ, to be used for reconstructing the secondary datum plane (Datum B). Datum B fixed the origin and direction of X axis (orthogonal to B). According to the same procedure, the third datum plane (Datum C) was identified on plane XZ, also setting the origin and direction of Y axis (orthogonal to C). This procedure is needed for establishing the positioning of the part in the CMM measurement area.

Moving to automatic control mode, using PC-Dmis 2021R2 software suite, the procedure above for DRF definition was repeated and a first estimation of parallelepiped dimensions was derived. The distance between opposite planes provided the dimensions of variables LX_{guess}, LY_{guess}, and LZ_{guess}, to be used for a more precise characterization. According to Fig. 2,

Table 2 Printing process parameters

Layer thickness	Saturation level	Bed temperature	Drying time	Recoater speed	Roller rotation speed	Roller transverse speed
50 µm	55%	55 °C	12 s	100 mm/s	600 rpm	5 mm/s

25 points were acquired on surfaces A and A2 (A2 opposite to A), 65 points on the surfaces B and B2, and 20–24 points on surfaces C and C2 (the range of points depends on the size of the hole). The position of the points to be measured was parametrically defined on the basis of the former estimation of sample dimensions. The more accurate reconstruction of planes A, B, and C served as a basis for final DRF definition. The remaining planes defining the boundary of the samples (A2, B2, C2) were reconstructed accordingly, and accurate linear dimensions (LX, LY and LZ) were determined.

Same approach was used for measuring the holes, starting from a first guess circle reconstructed by 12 points measured at equidistant angular position, with respect to the theoretical center. Seven circles were measured at equidistant levels on the cylindrical surface. The center of each circle was defined with respect to the guess circle, and 24 points were then measured at each level, to be used for precisely reconstructing the cylinder.

The complex measurement strategy above described has to be related to the expected large shrinkage on sintering, which significantly reduces the dimensions, so that the measurement of sintered samples cannot refer to the nominal CAD geometry of green parts. The parametric measurement procedure allows measuring both green and sintered parts, with no need for developing two distinct procedures. Moreover, the parametric approach allows determining a precise map of the local dimensional change on sintering, being the measured points symmetrically located on opposite planes, in the same position at both green and sintered state with respect to the boundary.

2.4 Microstructural analysis

The microstructure of the samples was analyzed by light optical microscopy and field-emission scanning electron microscopy (Zeiss Sigma 500 VP), both on polished and etched cross-sections, parallel to XY, XZ, and YZ planes, respectively. The micrographs obtained were used for the quantification of porosity and phase fraction through image analysis by ImageJ software. For both materials, two sets of samples were studied, namely ϕ3-L06 and ϕ5-L12, representative of the two extremes—the smallest hole closest to the building plane, the largest hole farthest from the building plane. The analysis was performed following specific patterns on the two classes of samples, as presented in Fig. 3, to minimize the risk of position-dependent results.

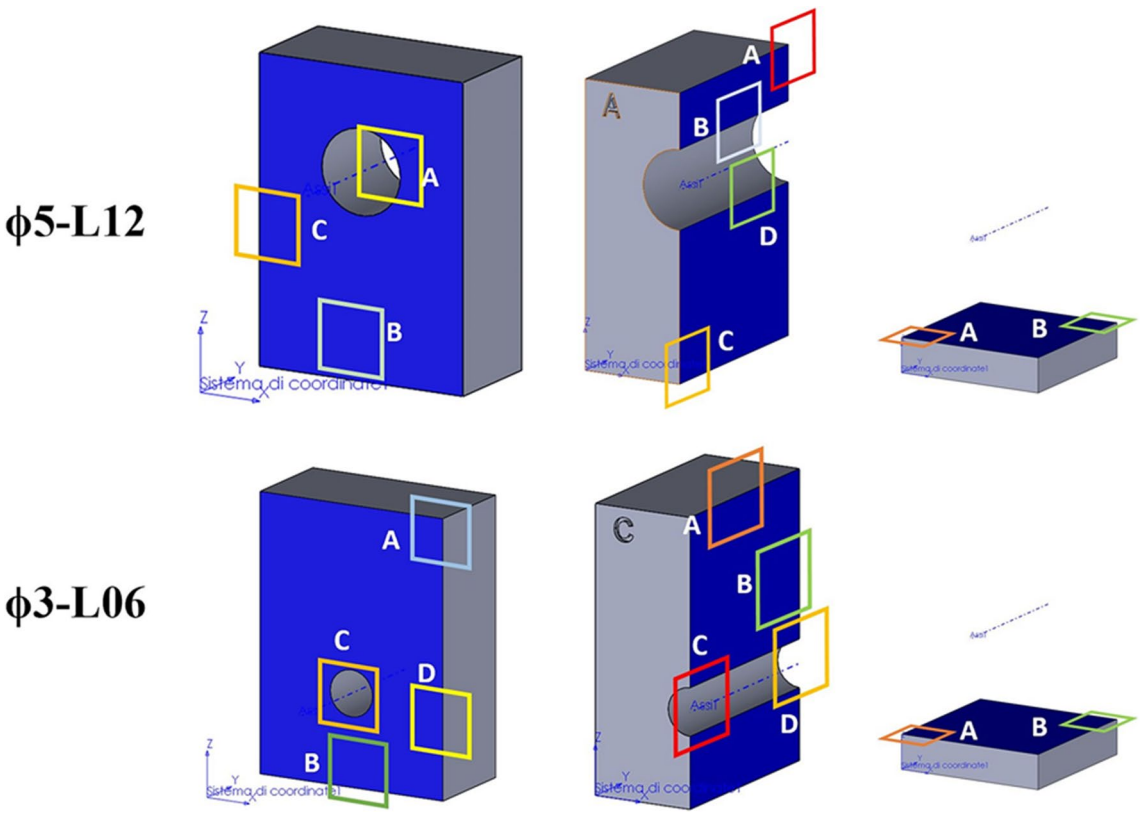

Fig. 3 Sections and locations analyzed by optical microscopy for 316L and 17-4PH samples

2.5 Evaluation of dimensional and geometrical variation

The dimensional changes on sintering of linear dimensions (ε_L) and diameters (ε_ϕ) were derived from the dimensions measured at green and sintered state by Eqs. (1) and (2), respectively.

$$\varepsilon_L = \frac{L_s - L_g}{L_g} \tag{1}$$

$$\varepsilon_\phi = \frac{\phi_s - \phi_g}{\phi_g} \tag{2}$$

where

- L corresponds to the linear dimension (LX, LY, LZ);
- ϕ corresponds to the diameter of reconstructed cylinder;
- g, s subscripts refer to the green and sintered state, respectively.

Assuming the volume of the sample (V) is equal to the difference between the volume of parallelepiped and cylindrical hole, as derived from measurements, the volumetric shrinkage (ε_V) was calculated by Eq. (3).

$$\varepsilon_V = \frac{V_s - V_g}{V_g} \tag{3}$$

To highlight the anisotropy of dimensional changes, normalized anisotropic coefficients were calculated by Eqs. (4) to (8). Equations (4) and (5) evaluate the ratio between the linear shrinkages in the building plane (ε_X; ε_Y) and the linear shrinkage along building direction (ε_Z). Equations (6) to (8) calculate the ratio between linear shrinkages and volumetric shrinkage, aiming at comparing the linear shrinkages of the two materials investigated, accounting for their different densification.

$$KL_{X/Z} = \frac{\varepsilon_X}{\varepsilon_Z} \tag{4}$$

$$KL_{Y/Z} = \frac{\varepsilon_Y}{\varepsilon_Z} \tag{5}$$

$$KV_{X/V} = \frac{\varepsilon_X}{\varepsilon_V} \tag{6}$$

$$KV_{Y/V} = \frac{\varepsilon_Y}{\varepsilon_V} \tag{7}$$

$$KV_{Z/V} = \frac{\varepsilon_Z}{\varepsilon_V} \tag{8}$$

The shrinkage of diameter experimentally derived (Eq. (2)) was compared to the shrinkage predicted by the model (Eq. (9)) described in [40], to be referred for deeper explanation. Equation (9) relates the shrinkage of the diameter of a hole (with the axis parallel to building plane and to Y direction) to the linear dimensional changes in X and Z directions.

$$\varepsilon_{\phi-model} = \frac{\varepsilon_z + 1}{2\pi} \int_0^{2\pi} \sqrt{1 - \frac{\left[\left(\varepsilon_z + 1\right)^2 - \left(\varepsilon_x + 1\right)^2\right]}{\left(\varepsilon_z + 1\right)^2} sin^2\alpha d\alpha} - 1 \tag{9}$$

where

- $\varepsilon_X, \varepsilon_Z$ represent the linear shrinkages along X and Z directions, respectively;
- α represents a parametric angular coordinate, which ranges between 0 and 2π.

The accuracy of the diameter shrinkage prediction was estimated by the normalized difference between the experimental and predicted diameter shrinkage, ε_ϕ and $\varepsilon_{\phi-model}$, respectively, by Eq. (10).

$$\Delta\varepsilon_\phi[\%] = 100 * \frac{\varepsilon_{\phi-model} - \varepsilon_\phi}{\varepsilon_\phi} \tag{10}$$

The geometrical accuracy of the hole was evaluated by the cylindricity form error. The empirical data were compared with the result of Eq. (11) where $\phi_g{\prime}$ is the nominal diameter of the cylinder at the green state (see [40] for deeper explanation).

$$cylindricityerror = \frac{1}{2}\phi_g{\prime}\left\{\left(\varepsilon_X + 1\right) - \left(\varepsilon_z + 1\right)\right\} \tag{11}$$

3 Results and discussion

The linear shrinkage of samples is firstly analyzed, and related to powder and binder spreading directions, and to the position of samples in the building plane. The diameter shrinkage and cylindricity form error are compared with the prediction of the analytical model. Finally, shape distortion is presented, and related to layer shifting during printing and to any density gradient along the sample height.

3.1 Linear dimensional change on sintering

Table 3 shows the linear dimensional change on sintering of LX, LY, and LZ. The dimensional change was calculated by Eq. (1) for each replicate, the averaged data and the standard deviation are reported in Table 3.

Table 3 Linear dimensional change on sintering – mean values and standard deviation

	ε_X [%] (dev.st)	ε_Y [%] (dev.st)	ε_Z [%] (dev.st)
316L	− 17.41 (0.20)	− 16.90 (0.13)	− 19.05 (0.23)
17-4PH	− 17.11 (0.19)	− 16.76 (0.20)	− 18.88 (0.29)

Table 3 highlights the anisotropic shrinkage along the three directions both in 316L and 17-4PH, and Table 4 reports the anisotropy coefficients calculated by Eqs. (4) to (8). The higher shrinkage along building direction (ε_Z) than in the building plane is reported in the literature, for stainless steel [24, 40, 43, 45], copper [46], superalloys [8], and ceramic [47] feedstocks. The anisotropic behavior is generally attributed to the layer-by-layer manufacturing process, which determines residual porosity between layers parallel to the building direction, as argued from the analysis of porosity evolution during sintering [48, 49]. Figure 4 shows the metallographic sections of 316L and 17-4PH perpendicular to the building direction. As explained by Cabo Rios et al. in [49], preparing a cross-section perfectly perpendicular to the building direction is challenging, and small inclination angle cannot be avoided. The layer-by-layer structure is however clearly highlighted, with high porosity bands representing the intersection between two deposition layers

Figure 4 shows finer, largely distributed pores in 316L (A) than in 17–4 PH (B), where pores appear larger and less distributed. This is likely due to the higher densification obtained in 17–4 PH, within the well-packed layers, in turn leading to significant pores coalescence among them.

Mostafaei et al. ascribed the higher shrinkage along Z direction to the influence of gravity on the rearrangement of powders after debinding, determining a denser configuration along Z direction [8]. Particle rearrangement during sintering is also considered by Wakai et al., relating the higher shrinkage along Z direction to the formation of new contacts between particles aligned with building direction [50]. Anisotropy coefficients KV, normalizing dimensional changes by the change in volume due to sintering, highlight the effect of printing. $KV_{Z/V}$ are exactly the same for the two materials, supporting the hypothesis that anisotropic dimensional change in Z direction has to be ascribed to printing, where the same parameters were used for both materials.

Aiming at highlighting the role of microstructure, further analysis has been performed. Figure 5 shows porosity and ferrite surface fractions, as resulting from micrographs analyzed in multiple areas (see Fig. 3), and Fig. 6 the pores and ferrite distributions, in the two materials.

The analysis in Fig. 5, obtained from multiple micrographs of different samples, highlights that overall porosity is slightly larger in 316L, while the ferritic fraction is higher in the 17-4PH steel. High magnification micrographs in Fig. 6 confirm that the ferrite phase is decorating the grain boundaries of the main phase in both materials, but in the case of 17-4PH (Fig. 6B) the secondary phase forms an almost continuous network surrounding the martensitic grains. The difference justifies the improved densification in 17–4 PH and the coalescence of voids, owing to the higher volume diffusivity typical of ferrite with respect to austenite at the sintering temperature.

Table 3 also shows the slightly higher shrinkage along X than Y direction, corresponding to the roller and printhead movement directions, respectively. The slight anisotropy in the X–Y plane can be ascribed to printing rather than sintering, as confirmed by the normalized anisotropic coefficients in Table 4, which are independent on densification. The small differences between the dimensional changes in the building plane were observed in literature for 316L metal powders; smaller dimensional changes along binder

Table 4 Anisotropy coefficients calculated by Eqs. (4) to (8) – mean values and standard deviation

	$KL_{X/Z}$ [%] (dev.st)	$KL_{Y/Z}$ [%] (dev.st)	$KV_{X/V}$ [%] (dev.st)	$KV_{Y/V}$ [%] (dev.st)	$KV_{Z/V}$ [%] (dev.st)
316L	91.40 (1.20)	88.73 (1.52)	39.18 (0.27)	38.03 (0.32)	42.87 (0.44)
17-4PH	90.64 (1.71)	88.80 (1.91)	38.88 (0.27)	38.09 (0.36)	42.91 (0.56)

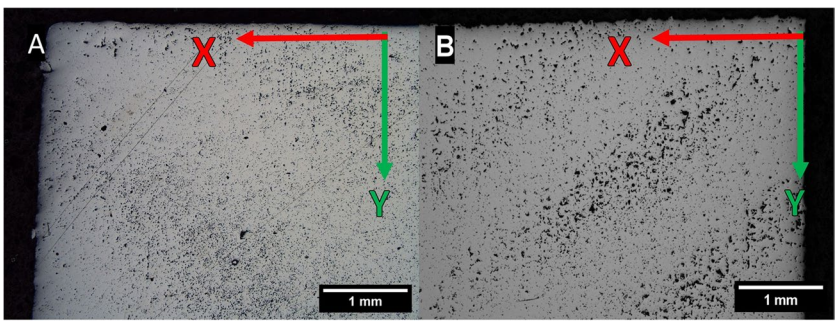

Fig. 4 Optical micrographs of ϕ5-L12 sintered samples showing interlayer residual porosity – sections nominally perpendicular to building direction – **A** 316L, **B** 17–4 PH

deposition direction (ε_y) were observed in [40, 51], while smaller dimensional changes along powder spreading direction (ε_x) were reported in [24, 43, 45]. Higher porosity clusters in parallel lines were reported in [51, 52], likely due to the high-velocity binder droplets impacting the powder bed, as observed by Parab et al. using high-speed synchrotron X-ray imaging [53]. Similar clusters are qualitatively observed in Fig. 7, showing residual porosity aligned along Y direction. The pores aligned along Y direction tend to almost complete closure during sintering, consequently determining higher densification, and dimensional change, along X direction. Future investigation should clarify the opposite anisotropic behavior observed in other papers.

The linear dimensional change on sintering is shown in Fig. 8a–c; the three graphs group the samples according to the position of the holes with respect to the building plane. On each graph, the three groups of bars refer to the dimensional changes in X, Y, and Z directions; blue shades correspond to 316L and red shades to 17-4PH, while different color bars represent the three sizes of holes.

Figure 8 confirms the largest dimensional change along building direction (Z) in the whole sampling, as well as the lower dimensional change in printhead movement direction (Y) with respect to powder spreading direction (X). In 316L, slightly lower dimensional changes are generally observed for samples with 4-mm diameter holes, on the contrary in 17-4PH samples with 4-mm diameter holes show the largest dimensional changes; no clear influence of position is observed. The differences are small, though

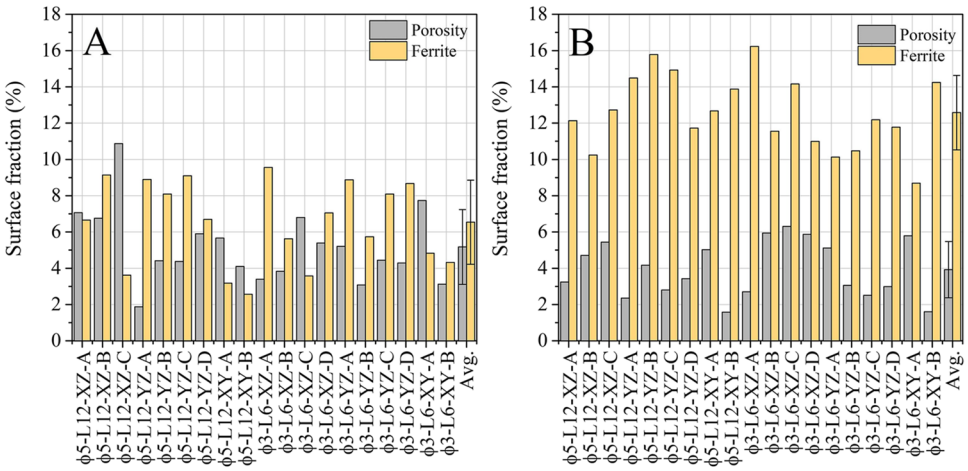

Fig. 5 Porosity and ferrite surface fractions obtained from micrographs in multiple areas of samples – **A** 316L, **B** 17–4 PH

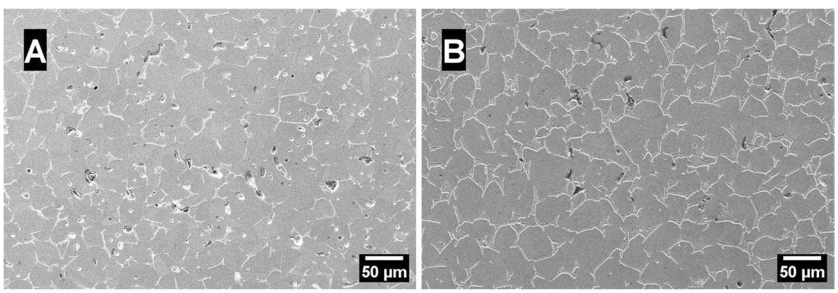

Fig. 6 Pores and ferrite distributions in ϕ3-L06 sections nominally perpendicular to building direction – **A** 316L, **B** 17–4 PH

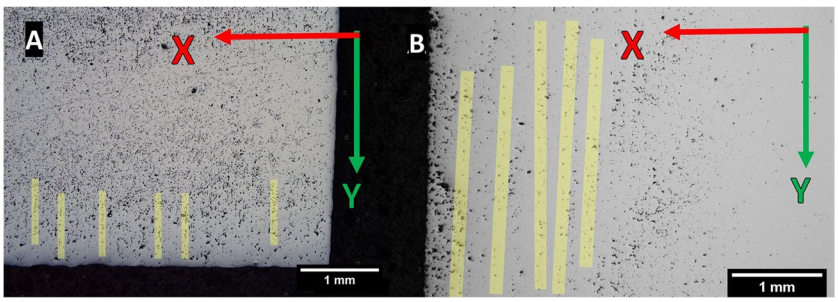

Fig. 7 Optical micrographs of sintered samples showing residual porosity aligned along Y direction (binder injection deposition) – sections nominally perpendicular to building direction – **A** 316L (ϕ5-L12), **B** 17-4PH (ϕ3-L06)

not always negligible. The results above will be further considered on the basis of the analysis of shape distortion.

The influence of samples position in the printing plane is investigated below.

Figures 9 and 10 plot the relative density and the volumetric shrinkage of the whole sampling with respect to the position in the building plane. Each bar represents a single sample, as explained in paragraph 2.1.

The two materials experienced different densification: as shown in Figs. 9, 17-4PH achieved higher average relative density. The lower densification observed in 316L is likely to be ascribed to the actual time at isothermal temperature during sintering of 316L, which is the same for the two materials, but shorter with respect to the optimized treatment presented in previous studies [54].

The volume shrinkage, instead, which is generally slightly higher for 316L, might be related to particles packing and distribution, as highlighted by the microstructural analysis, rather than to the evolution during final sintering step. Nevertheless, the influence of printing on volumetric shrinkage can be highlighted for both materials. Volumetric shrinkage of 316L is higher in the center of the building box, and strongly decreases moving towards the extreme positions of printhead movement (along Y axis). 17-4PH volumetric shrinkage is more uniform, slightly decreasing moving to the upper limit of printhead movement direction, as also observed in 316L. The different volumetric shrinkage

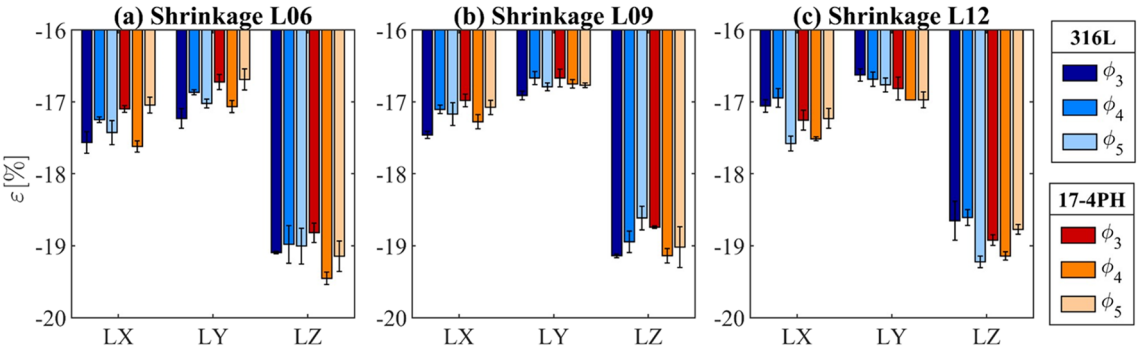

Fig. 8 Linear dimensional change on sintering as affected by the hole diameter (ϕ3, ϕ4, ϕ5) and axis position (L06, L09, L12)) – error bars represent one sigma standard deviation

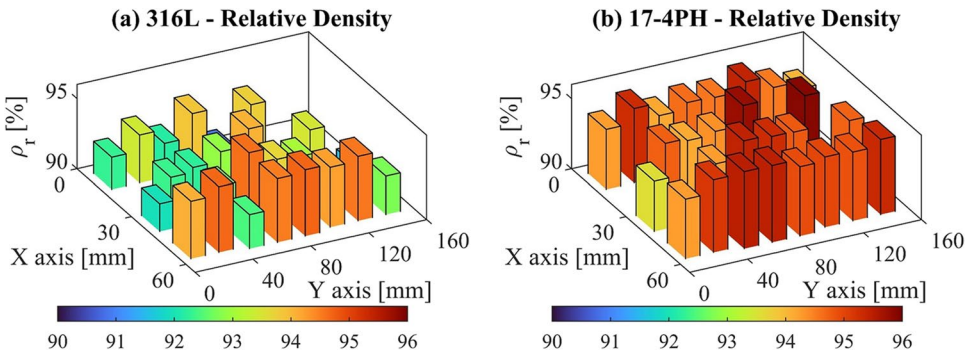

Fig. 9 Relative density of **a** 316L and **b** 17-4PH samples according to the position in the building plane

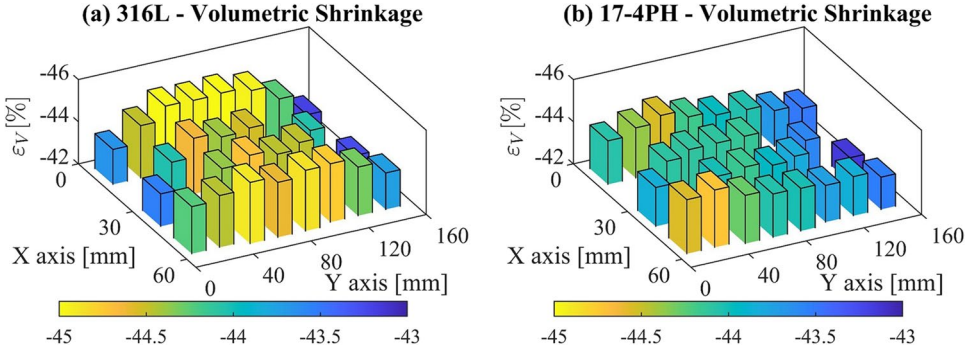

Fig. 10 Volumetric shrinkage of **a** 316L and **b** 17-4PH samples according to the position in the building plane

is certainly affected by the different green density, in turn influenced by the printing parameters, according to recent work. Lower volumetric shrinkage related to higher green density has been presented by Chen et al. as the result of numerical simulation [55], and experimentally confirmed by Barthel et al. [10]. Inhomogeneous green density as a function of the position in the building plane was highlighted by Lores et al., reporting that green density decreases close to the border of the building box; the strongest decrease was observed close to maximum Y coordinate (Y 160 mm) [56]. Green density is also affected by drying time [57, 58] and saturation level [59, 60]. The variations of volumetric shrinkage observed in this work along printhead movement direction (Y) could be related to slight variations in binder injection, meaning saturation level, and/or to variations in the heat transmitted by the heating lamp moving along Y axis, meaning drying unit.

3.2 Dimensional change on sintering of diameters

The dimensional change on sintering of diameters is shown Fig. 11 comparing the real shrinkage, derived from measurement according to Eq. (2), to the shrinkage predicted by the model. The predicted shrinkage of diameters was derived from Eq. (9) introducing the measured linear dimensional changes presented above, which are specific for each geometry, as shown in Fig. 8. Model prevision error is shown by the difference between predicted and measured dimensional change normalized by the measured dimensional change, calculated by Eq. (10). Positive values are related to shrinkage over-estimation, while negative to underestimation.

Data are gathered by the position of the hole (L06, L09, L12), blue shades correspond to 316L and red shades to 17-4PH, while different color bars refer to the three sizes of holes.

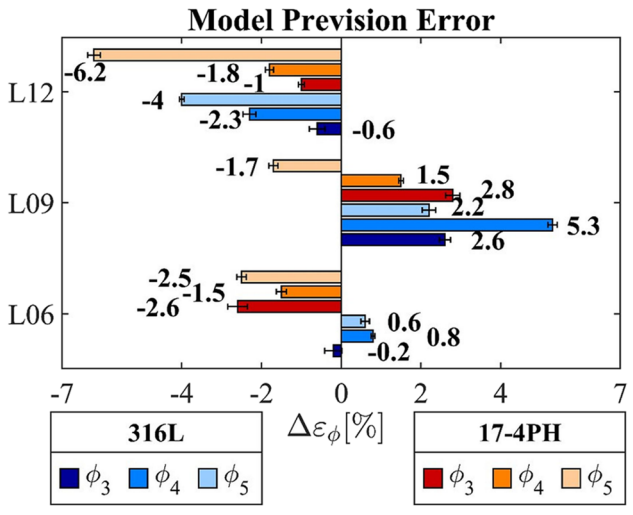

Fig. 11 Normalized difference between the predicted and experimental shrinkage of diameters calculated by Eq. (10)

Despite no clear trend can be recognized, neither depending on material, nor on diameter, or hole position, Fig. 11 shows quite good agreement between experimental and predicted values. Average discrepancy is below 3%, while maximum error exceeds 4% just in three cases; the best results are obtained for 316L samples with the hole closest to the building plane.

In previous work, the larger discrepancy between measured and predicted values was observed for the smallest 3-mm holes, being less significant for larger holes [40, 61]. The mass of powder over the cylinder section was expected to deform the holes by gravity load effect, combined with the viscous-plastic behavior of the material during sintering, thus affecting the shrinkage of diameters and determining the difference with respect to the values predicted by the model. Figure 12 shows the metallographic cross-section of hole cavities. Samples with the smallest holes closest to the building plane are shown (A and B), along with samples with the largest holes farthest from the building plane (C and D). Aiming at keeping the same magnification, and making the comparison with A and B easier, only the profile of the upper part of the holes is shown in the case of samples C and D, the most representative for gravity load effect.

A slight distortion can be recognized in the upper surface along the hole axis in samples A and B, confirming the influence of gravity load effect, despite the small differences due to the slightly different positions of the section plane (in deeper position in sample B than in sample A, so that the dimension in Z direction has not to be considered as representative of the diameter). The position of the holes is the closest to the building plane, so that the mass above is the largest, and consequently the effect of the gravity load. No distortion is observed in samples C and D, the farthest from the building plane, with the lowest mass above, and consequently the lowest gravity load effect. The profile of the holes cross section is in fact parallel to the profile of the upper surface, which is visible in the upper side in pictures C and D.

Cylindricity form error at green and sintered state is shown in Fig. 13, along with model prevision calculated by Eq. (11). Data are gathered by the position of the hole (L06, L09, L12), blue shades correspond to the three sizes of the holes in 316L, and red shades to the three sizes of the holes in 17–4 PH.

At the green state, cylindricity form error is generally lower than 0.1 for both materials in the whole sampling, slightly increasing with the size of the hole, almost unaffected by the position.

At the sintered state cylindricity form error is close to 0.15 mm, for both materials in the whole sampling, except for the largest holes (ϕ5). Similar results were obtained in

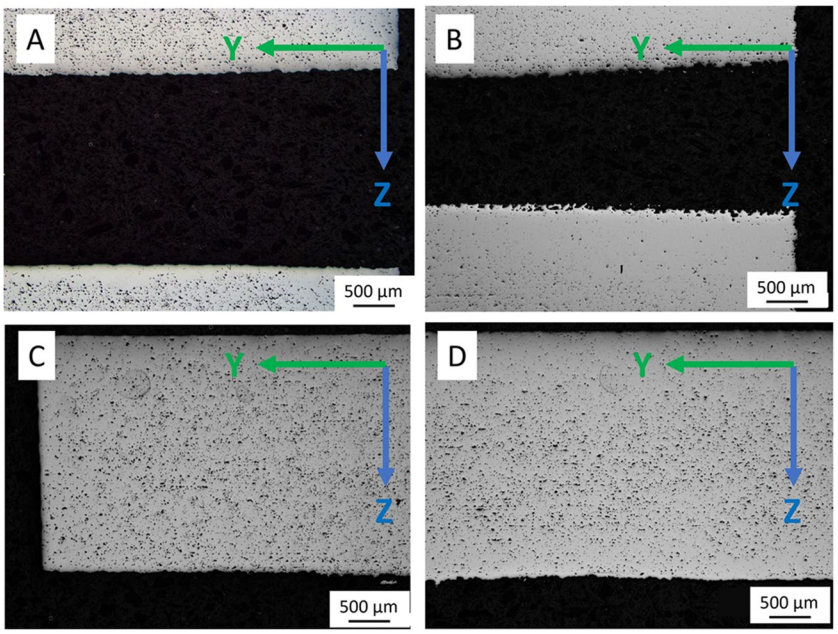

Fig. 12 Longitudinal section of holes of sintered samples – sections on YZ planes – ϕ3-L06—**A** 316L, **B** 17-4PH; ϕ5-L12—**C** 316L, **D** 17-4PH

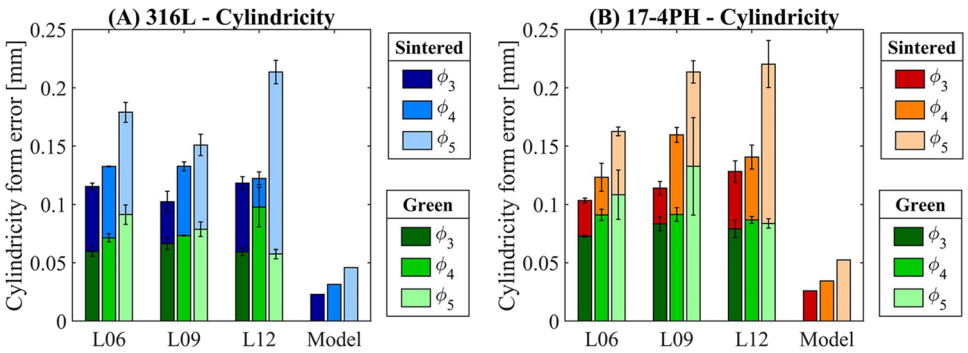

Fig. 13 Cylindricity form error measured at green and sintered state along with cylindricity form error derived from analytical model (Eq. (11)) – **A** 316L, **B** 17-4PH

the previous work [40], and by Dahmen et al. using X-ray tomography and computer image reconstruction [39]. For 316L, minimum cylindricity form error is related to L09 position for any size, except for holes ϕ4, whose cylindricity is almost constant, unaffected by the position. For 17–4 PH, minimum cylindricity form error is related to L06 position for any size. Concerning the size, cylindricity form error tends to increase on increasing diameter, confirming the trend predicted by the model.

The above results confirm that cylindricity form error at sintered state is due both to form error at green state, and to the detrimental effect of the anisotropic shrinkage on sintering. Both the diameter shrinkage and cylindricity form error deviate from the prediction of the model, which is only based on the effect of anisotropic dimensional change on sintering. Nevertheless, printing process can also significantly affect geometrical characteristics, due to layer-by-layer fabrication [18], CAD conversion into STL file, inhomogeneity in the material, and control of the printing process [33]. Aiming at considering the printing process along with the anisotropic dimensional change on sintering in determining the geometrical characteristics of the holes, the cylindricity form error at the green state can be added to the form error expected by the model, as shown in Fig. 14.

The resulting difference between the actual form error at sintered state and the expected one is considerably lowered, and eliminated in the case of the 17–4 PH samples with holes closest to the building plane. However, the difference between the actual form error at sintered state and the expected one is still significant in the other samples, mainly in the case of large holes far from the building plane. The contribution of shape distortion of parallelepiped geometry should have determined the resulting shape error and diameter shrinkage, as described in the next section.

3.3 Shape distortion

Aiming at highlighting the shape distortion of the parallelepiped geometry of the sintered parts, Figs. 15 and 16 show the shape of the planes orthogonal to the building direction,

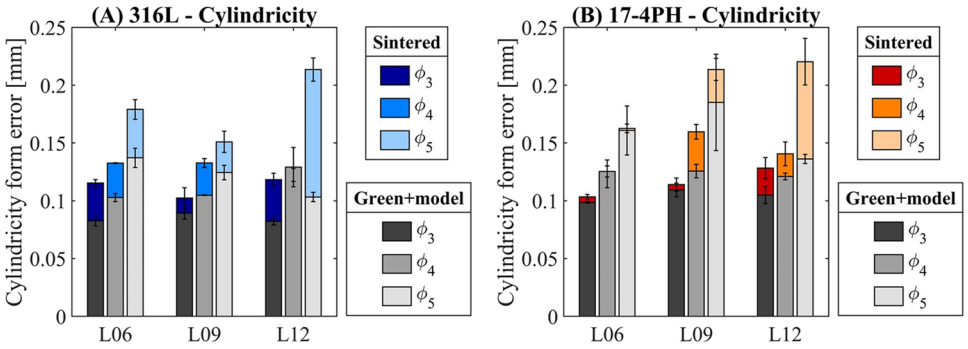

Fig. 14 Cylindricity form error measured at green state added with cylindricity form error derived from analytical model compared to cylindricity form error at sintered state – **A** 316L, **B** 17-4PH

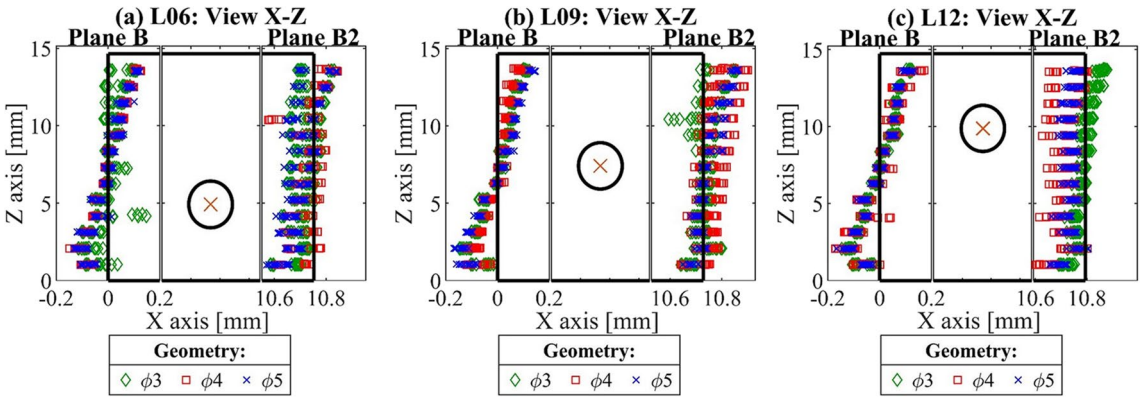

Fig. 15 Front view (X–Z) of the nominal sample geometries at sintered state. **a** L06, **b** L09, **c** L12. Symbols represent the points measured by CMM on planes B and B2, on different replicates of 316L samples with holes ϕ3, ϕ4, ϕ5, projected on X–Z view

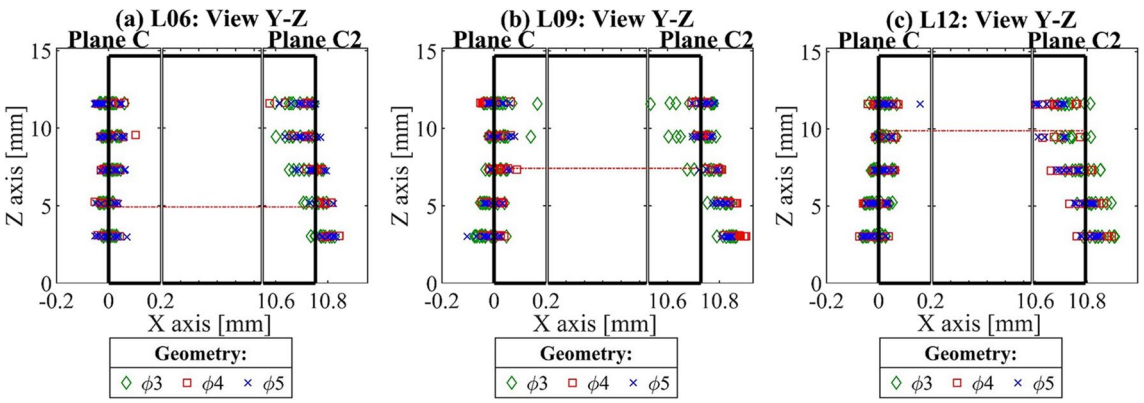

Fig. 16 Side view (Y–Z) of the nominal sample geometries at sintered state – red dotted lines represent the axes of the holes. **a** L06, **b** L09, **c** L12. Symbols represent the points measured by CMM on planes C and C2, on different replicates of 316L samples with holes ϕ3, ϕ4, ϕ5, projected on Y–Z view

B-B2 and C-C2 respectively, as derived from the measured points at sintered state for 316L; the same is shown for 17–4 PH in Figs. 17 and 18.

As an example, Fig. 15a–c shows the front view of L06, L09, and L12 geometries reporting the points measured by the CMM on planes B and B2 on samples with different holes diameter (ϕ3 green rhombi, ϕ4 red squares, ϕ5 blue crosses). The measured points are projected on X–Z view, enlarging the scale close to the nominal edge of the geometry to highlight the distortion of the real surfaces. All the points measured on the three replicates for each geometry is shown collectively.

Figures 15 and 17 show that for both materials planes B and B2 are significantly tilted towards X direction (powder

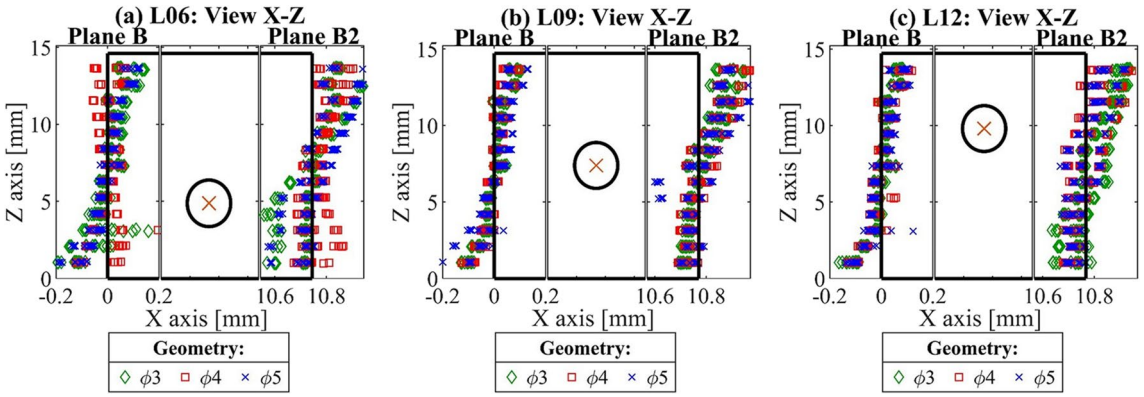

Fig. 17 Front view (X–Z) of the nominal sample geometries at sintered state. **a** L06, **b** L09, **c** L12. Symbols represent the points measured by CMM on planes B and B2, on different replicates of 17-4PH samples with holes ϕ3, ϕ4, ϕ5, projected on X–Z view

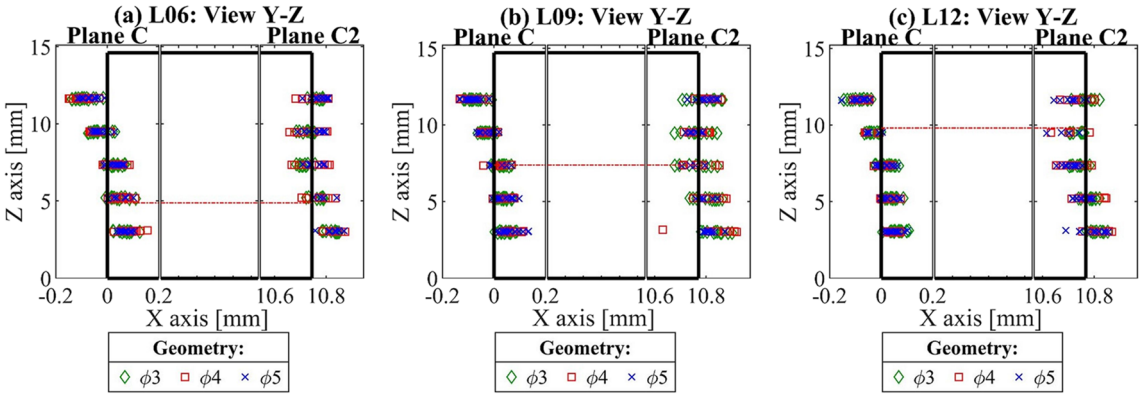

Fig. 18 Side view (Y–Z) of the nominal sample geometries at sintered state – red dotted lines represent the axes of the holes. **a** L06, **b** L09, **c** L12. Symbols represent the points measured by CMM on planes C and C2, on different replicates of 17-4PH samples with holes ϕ3, ϕ4, ϕ5, projected on Y–Z view

spreading direction); therefore, the discrepancy of the surfaces from the nominal profile could be related to the effect of layer shifting during the printing operation. The effect is not as evident as in previous work [62]; however, the drift at sintered state is observed in the whole sampling, confirming the influence of layer shifting in powder spreading direction, enhanced on sintering. The shape distortion above highlighted, determining the discrepancy from the nominal parallelepiped shape, increases along the building direction, and can be related to the generally higher cylindricity form error observed in the holes far from the building plane.

Shape distortion after sintering shown in Figs. 16 and 18, instead, is trapezoidal/hourglass-shaped. The trapezoidal shape can be ascribed to the frictional forces acting on sintering between samples and trays during sintering. Frictional forces could counteract the sintering force which determines the shrinkage, consequently lower close to the base of the sample. Additional effect due to gravity load might be hypothesized, as observed in Fig. 12.

The hourglass shape has different interpretation, possibly ascribed to different densification along the sample height: higher in the middle, lower at the extreme positions.

3.4 Phenomena determining the dimensional/geometrical accuracy with respect to the geometry of parts

The above results highlight the complexity of developing reliable predictive models for dimensional change on sintering of MBJ parts, due to the many different phenomena occurring during printing and sintering. Layer shifting and binder distribution during printing enhance the shape distortion during sintering, in turn affected by the size/position of the holes.

Distinguishing the different contributions is difficult, and both position and size play significant role, as described below.

In the holes closest to the building plane (L06), the larger gravity load effect due to the higher mass of powder above

might enhance shrinkage, but the counteracting frictional forces with trays might determine lower shrinkage, and layer shifting effect is also lower close to the building plane. The counteracting effects are balanced, so that the main effect determining shrinkage is the anisotropic dimensional change on sintering predicted by the model, thus resulting in very accurate prediction of size and cylindricity. The difference between real and predicted diameter is lower than 1% for 316L and around 2% for 17–4 PH (Fig. 11), where slightly larger gravity load effect was observed (Fig. 12). Cylindricity is also precisely predicted, less than 0.05 mm underestimation in 316L and even less in 17–4 PH (Fig. 14).

In the holes positioned in the middle of the samples (L09), the effect of both gravity and frictional forces is lower, while shape deformation prevails. The effect is noticeable in 316L with ϕ4 hole, where the difference between real and predicted diameter increases up to 5% (Fig. 11) and the effect of layer shifting is evident (red squares in Fig. 15b). It has to be recalled that mean linear shrinkages, derived from distances between opposed surfaces, determine the predicted dimensional change of diameter (Eq. (9)), so that any shape distortion markedly affects the reliability of prediction. In the other samples with holes positioned in the middle, the influence of shape deformation is lower, and the prediction of diameters is very accurate; the difference between real and predicted diameter is around 2% for both materials (Fig. 11). Cylindricity is also precisely predicted, less than 0.05 mm underestimation for both materials (Fig. 14).

In the position at the largest distance from the building plane (L12), no effect of gravity load (Fig. 12C and D) neither of frictional forces with trays can be argued, while strong effect of shape deformation is observed. The effect is highly remarkable in the largest holes (ϕ5), where size is underestimated by 4 ÷ 6% (Fig. 11) and cylindricity underestimation is up to 0.1 mm, due to layer shifting effect.

4 Conclusions

This work investigated the dimensional and geometrical accuracy and precision of AISI 316L and 17–4 PH samples fabricated by MBJ, characterized by a through hole with the axis parallel to the building plane, differing for diameter (3, 4, 5 mm), and position of the axis with respect to the building plane (6, 9, 12 mm distance). The dimensions and shape of parts at green and sintered state were obtained from the surfaces reconstructed by the points measured with a coordinate measuring machine. Linear dimensional changes and geometrical characteristics were derived accordingly.

Linear dimensional changes on sintering are anisotropic for both materials. Higher shrinkage occurs along building direction (Z) – 18.5 ÷ 19.5%, than in the building plane – 15.5 ÷ 17.5%, as generally observed in literature. In addition, slightly higher shrinkage – 0.5 ÷ 0.8% was measured along powder spreading direction (X) than binder injection direction (Y), due to the inhomogeneous porosity distribution determined by droplets deposition method. Anisotropy coefficients normalized by the change in volume allowed to highlight the contribution of printing to anisotropic dimensional changes. The change in volume depends on the position of samples in the building plane due to variation in green density (up to 3% in relative density in 316L).

The dimensional change of diameters generally confirmed the expected shrinkage based on the analytical model described in previous work. The difference between real and expected dimensional changes is lower than 3%, except for two geometries (4 ÷ 6%), due to the different contribution of the phenomena responsible for shrinkage. The cylindricity form error evaluated with the prediction model for anisotropic dimensional changes on sintering was strongly underestimated (up to 0.15 mm in the worst cases), but underestimation was considerably reduced (generally lower than 0.05 mm) adding the cylindricity form error due to printing. The analysis of dimensional changes of diameters along with cylindricity form error highlighted the role of gravity load and frictional forces with trays during sintering as prevailing effects for holes closest to the building plane, and the role of shape distortion during sintering (in turn related to layer shifting) as prevailing effect for holes furthest from the building plane.

A significant deviation from nominal parallelepiped geometry was observed for both materials, strongly affecting dimensional changes and geometrical characteristics. Planes orthogonal to powder spreading direction are distorted since sintering enhances the layer shifting error produced during printing. Moreover, the overall trapezoidal shaped distortion can be ascribed to the influence of frictional force acting between support trays and sample surfaces during sintering. Additional effect due to gravity was observed sectioning the holes closest to the building surface, coherently with the observed shape distortion.

This work clearly showed that dimensional and geometrical accuracy of MBJ parts results from different phenomena, whose effects also depend on the geometry of the part. The model developed in previous work allows predicting the anisotropic dimensional change on sintering, and will be further implemented with the knowledge gained in this study. The work also highlighted the complexity of the topic, and the need for further analysis on the effect of the printing parameters, to be optimized, depending on the geometry of the part. Future work will develop factors describing the influence of gravity load, frictional forces, layer shifting, and inhomogeneous density as functions of the geometry of the parts, again to be implemented in the prediction model. The improved model will be developed in a design procedure to be used for precisely modeling the geometry of MBJ parts, aiming at obtaining final

parts fulfilling the dimensional and geometrical requirements, minimizing or eliminating secondary operations. The procedure will be of high interest for companies producing MBJ parts with strict dimensional and geometrical requirements, as in automotive field, toolmaking and luxury consumer goods, whose characteristics cannot be obtained simply applying scaling factors to the nominal geometry.

Author contribution All authors contributed to the study conception and design. The preparation of printed and sintered samples was performed by Nora Lecis and Marco Mariani, measurement of samples and data collection were performed by Marco Zago and Marco Mariani. The analysis and discussion of results was performed by all the authors. The first draft of the manuscript was written by Marco Zago; all authors commented on previous versions of the manuscript. The revised manuscript was written by Ilaria Cristofolini. All authors read and approved the revised manuscript.

Funding Open access funding provided by Università degli Studi di Trento within the CRUI-CARE Agreement.

Data availability The authors declare that the data supporting the findings of this study are available within the paper, clearly recognizable in tables and figures.

Code availability Not applicable.

Declarations

Ethics approval The authors state that the research did not involve vulnerable participants, minors, clinical patients, human tissue, animals, human biological material, and genetically modified organisms.

Consent to participate The authors understand that my manuscript and associated personal data will be shared with Research Square for the delivery of the author dashboard.

Consent for publication The authors agree with the Copyright Transfer Statement.

Conflict of interest The authors declare no competing interests.

References

1. Chadha U, Abrol A, Vora NP et al (2022) Performance evaluation of 3D printing technologies: a review, recent advances, current challenges, and future directions. Prog Addit Manuf 7:853–886. https://doi.org/10.1007/s40964-021-00257-4
2. Li M, Du W, Elwany A, Pei Z, Ma C (2020) Metal binder jetting additive manufacturing: a literature review. J Manuf Sci Eng 142:1–17. https://doi.org/10.1115/1.4047430
3. Ziaee M, Crane NB (2019) Binder jetting: a review of process, materials, and methods. Addit Manuf 28:781–801. https://doi.org/10.1016/j.addma.2019.05.031
4. Lores A, Azurmendi N, Agote I, Zuza E (2019) A review on recent developments in binder jetting metal additive manufacturing: materials and process characteristics. Powder Metall 62:267–296. https://doi.org/10.1080/00325899.2019.1669299
5. Mostafaei A, Elliott AM, Barnes JE et al (2021) Binder jet 3D printing—process parameters, materials, properties, modeling, and challenges. Prog Mater Sci 119:100707. https://doi.org/10.1016/j.pmatsci.2020.100707
6. German RM (1992) Prediction of packing and sintering density for bimodal powder mixtures. Adv Powder Metall 3:1–15. https://doi.org/10.1016/0026-0657(93)92034-3
7. Bai Y, Wagner G, Williams CB (2017) Effect of particle size distribution on powder packing and sintering in binder jetting additive manufacturing of metals. J Manuf Sci Eng Trans ASME 139:1–15. https://doi.org/10.1115/1.4036640
8. Mostafaei A, Rodriguez De Vecchis P, Nettleship I, Chmielus M (2019) Effect of powder size distribution on densification and microstructural evolution of binder-jet 3D-printed alloy 625. Mater Des 162:375–383. https://doi.org/10.1016/j.matdes.2018.11.051
9. Rishmawi I, Salarian M, Vlasea M (2018) Tailoring green and sintered density of pure iron parts using binder jetting additive manufacturing. Addit Manuf 24:508–520. https://doi.org/10.1016/j.addma.2018.10.015
10. Barthel B, Janas F, Wieland S (2021) Powder condition and spreading parameter impact on green and sintered density in metal binder jetting. Powder Metall 64(5):378–386. https://doi.org/10.1080/00325899.2021.1912923
11. Crane NB (2020) Impact of part thickness and drying conditions on saturation limits in binder jet additive manufacturing. Addit Manuf 33:101127. https://doi.org/10.1016/j.addma.2020.101127
12. Colton T, Inkley C, Berry A, Crane NB (2021) Impact of inkjet printing parameters and environmental conditions on formation of 2D and 3D binder jetting geometries. J Manuf Process 71:187–196. https://doi.org/10.1016/j.jmapro.2021.09.024
13. Vaezi M, Chua CK (2011) Effects of layer thickness and binder saturation level parameters on 3D printing process. Int J Adv Manuf Technol 53:275–284. https://doi.org/10.1007/s00170-010-2821-1
14. Kafara M, Kemnizter J, Westermann H-H, Steinhilper R (2018) Influence of binder quantity on dimensional accuracy and resilience in 3D printing. Procedia Manuf 21:638–646. https://doi.org/10.1016/j.promfg.2018.02.166
15. Yamaguchi D, Oya N (2022) In situ visualization of aluminum sintering for binder jetting by X-ray transmission. Int J Adv Manuf Technol 121:3965–3975. https://doi.org/10.1007/s00170-022-09601-6
16. Yamaguchi D, Oya N (2023) X-ray observation study of the influence of binder deposition on sintering process of aluminum binder jetting. Int J Adv Manuf Technol 128:1981–1990. https://doi.org/10.1007/s00170-023-12058-w
17. Simchi A, Petzoldt F, Hartwig T et al (2023) Microstructural development during additive manufacturing of biomedical grade Ti-6Al-4V alloy by three-dimensional binder jetting: material aspects and mechanical properties. Int J Adv Manuf Technol 127:1541–1558. https://doi.org/10.1007/s00170-023-11661-1

18. Ratnadeep P, Anand S (2011) Optimal part orientation in Rapid Manufacturing process for achieving geometric tolerances. J Manuf Syst 30(4):214–222. https://doi.org/10.1016/j.jmsy.2011.07.010
19. Khoshkhoo A, Carrano AL, Blersch DM (2018) Effect of build orientation and part thickness on dimensional distortion in material jetting processes. Rapid Prototyping J 24(9):1563–1571. https://doi.org/10.1108/RPJ-10-2017-0210
20. Vitolo F, Martorelli M, Gerbino S et al (2018) Controlling form errors in 3D printed models associated to size and position on the working plane. Int J Interact Des Manuf 12:969–977. https://doi.org/10.1007/s12008-017-0441-9
21. Lee Y, Gurnon AK, Bodner D, Simunovic S (2020) Effect of particle spreading dynamics on powder bed quality in metal additive manufacturing. Integr Mater Manuf Innov 9:410–422. https://doi.org/10.1007/s40192-020-00193-1
22. Wang Y, Zhao YF (2017) Investigation of sintering shrinkage in binder jetting additive manufacturing process. Procedia Manuf. 10:779–790. https://doi.org/10.1016/j.promfg.2017.07.077
23. Do T, Kwon P, Shin CS (2017) Process development toward full-density stainless steel parts with binder jetting printing. Int J Mach Tools Manuf 121:50–60. https://doi.org/10.1016/j.ijmachtools.2017.04.006
24. Cabo Rios A, Hryha E, Olevsky E, Harlin P (2021) Sintering anisotropy of binder jetted 316L stainless steel: part I–sintering anisotropy. Powder Metall 65(4):273–282. https://doi.org/10.1080/00325899.2021.2020485
25. Schmutzler C, Stiehl TH, Zaeh MF (2019) Empirical process model for shrinkage-induced warpage in 3D printing. Rapid Prototyping J 25(4):721–727. https://doi.org/10.1108/RPJ-04-2018-0098
26. Zhang K, Zhang W, Brune R et al (2021) Numerical simulation and experimental measurement of pressureless sintering of stainless steel part printed by Binder Jetting Additive Manufacturing. Addit Manuf 47:102330. https://doi.org/10.1016/j.addma.2021.102330
27. Paudel BJ, Conover D, Lee JK, To AC (2021) A computational framework for modeling distortion during sintering of binder jet printed parts. J Micromechanics Mol Phys 6:95–102. https://doi.org/10.1142/S242491302142008X
28. SadeghiBorujeni S, Shad A, Abburi Venkata K et al (2022) Numerical simulation of shrinkage and deformation during sintering in metal binder jetting with experimental validation. Mater Des 216:110490. https://doi.org/10.1016/j.matdes.2022.110490
29. Lee Y, Nandwana P, Simunovic S (2021) Powder spreading, densification, and part deformation in binder jetting additive manufacturing. Prog Addit Manuf 7(1):111–125. https://doi.org/10.1007/s40964-021-00214-1
30. Stevens E, Schloder S, Bono E et al (2018) Density variation in binder jetting 3D-printed and sintered Ti-6Al-4V. Addit Manuf 22:746–752. https://doi.org/10.1016/j.addma.2018.06.017
31. Sahli M, Lebied A, Gelin JC et al (2015) Numerical simulation and experimental analysis of solid-state sintering response of 316 L stainless steel micro-parts manufactured by metal injection molding. Int J Adv Manuf Technol 79:2079–2092. https://doi.org/10.1007/s00170-015-6983-8
32. Mostafaei A, Stevens EL, Ference JJ et al (2018) Binder jetting of a complex-shaped metal partial denture framework. Addit Manuf 21:63–68. https://doi.org/10.1016/j.addma.2018.02.014
33. Huang Z, Dantan JY, Etienne A et al (2018) Geometrical deviation identification and prediction method for additive manufacturing. Rapid Prototyp J 24:1524–1538. https://doi.org/10.1108/RPJ-07-2017-0137
34. Borujeni SS, Saluja GS, Ploshikhin V (2023) Compensation of sintering deformation for components manufactured by metal binder jetting using numerical simulations. Rapid Prototyping J 29(3):612–625. https://doi.org/10.1108/RPJ-06-2022-0181
35. Paudel BJ, Deng H, To AC (2023) A physics-based data-driven distortion compensation model for sintered binder jet parts considering size effects. Addit Manuf 68:103517. https://doi.org/10.1016/j.addma.2023.103517
36. Arni R, Gupta SK (2001) Manufacturability analysis of flatness tolerances in solid freeform fabrication. J Mech Des Trans ASME 123:148–156. https://doi.org/10.1115/1.1326439
37. Islam MN, Sacks S (2016) An experimental investigation into the dimensional error of powder-binder three-dimensional printing. Int J Adv Manuf Technol 82:1371–1380. https://doi.org/10.1007/s00170-015-7482-7
38. Ollison T, Berisso K (2010) Three-dimensional printing build variables that impact cylindricity. J Ind Technol 26:1–10
39. Dahmen T, Klingaa CG, Baier-Stegmaier S et al (2020) Characterization of channels made by laser powder bed fusion and binder jetting using X-ray CT and image analysis. Addit Manuf 36:101445. https://doi.org/10.1016/j.addma.2020.101445
40. Zago M, Lecis NFM, Vedani M, Cristofolini I (2021) Dimensional and geometrical precision of parts produced by Binder Jetting process as affected by the anisotropic shrinkage on sintering. Addit Manuf 43:102007. https://doi.org/10.1016/j.addma.2021.102007
41. Zago M, Lecis N, Mariani M et al (2023) Influence of shape distortion on the precision of holes in parts fabricated by Metal Binder Jetting. Int J Interact Des Manuf. https://doi.org/10.1007/s12008-023-01357-x
42. Miyanaji H, Momenzadeh N, Yang L (2018) Effect of printing speed on quality of printed parts in Binder Jetting Process. Addit Manuf 20:1–10. https://doi.org/10.1016/j.addma.2017.12.008
43. Lecis N, Mariani M, Beltrami R et al (2021) Effects of process parameters, debinding and sintering on the microstructure of 316L stainless steel produced by binder jetting. Mater Sci Eng A 828:142108. https://doi.org/10.1016/j.msea.2021.142108
44. Vora HD, Sanyal S (2020) A comprehensive review: metrology in additive manufacturing and 3D printing technology. Prog Addit Manuf 5:319–353. https://doi.org/10.1007/s40964-020-00142-6
45. Ziaee M, Tridas EM, Crane NB (2017) Binder-jet printing of fine stainless steel powder with varied final density. Jom 69:592–596. https://doi.org/10.1007/s11837-016-2177-6
46. Miyanaji H, Rahman KM, Da M, Williams CB (2020) Effect of fine powder particles on quality of binder jetting parts. Addit Manuf 36:101587. https://doi.org/10.1016/j.addma.2020.101587
47. Gonzalez JA, Mireles J, Lin Y, Wicker RB (2016) Characterization of ceramic components fabricated using binder jetting additive manufacturing technology. Ceram Int 42:10559–10564. https://doi.org/10.1016/j.ceramint.2016.03.079
48. Zhu Y, Wu Z, Hartley WD et al (2020) Unraveling pore evolution in post-processing of binder jetting materials: X-ray computed tomography, computer vision, and machine learning. Addit Manuf 34:101183. https://doi.org/10.1016/j.addma.2020.101183
49. Cabo Rios A, Hryha E, Olevsky E, Harlin P (2021) Sintering anisotropy of binder jetted 316L stainless steel: part II–microstructure evolution during sintering. Powder Metall 65(4):283–295. https://doi.org/10.1080/00325899.2021.2020486
50. Wakai F, Chihara K, Yoshida M (2007) Anisotropic shrinkage induced by particle rearrangement in sintering. Acta Mater 55:4553–4566. https://doi.org/10.1016/j.actamat.2007.04.027
51. Jamalkhani M, Asherloo M, Gurlekce O et al (2022) Deciphering microstructure-defect-property relationships of vacuum-sintered binder jetted fine 316L austenitic stainless steel powder. Addit Manuf 59:103133. https://doi.org/10.1016/j.addma.2022.103133
52. Mostafaei A, Stevens EL, Hughes ET et al (2016) Powder bed binder jet printed alloy 625: Densification, microstructure and

mechanical properties. Mater Des 108:126–135. https://doi.org/10.1016/j.matdes.2016.06.067
53. Parab ND, Barnes JE, Zhao C et al (2019) Real time observation of binder jetting printing process using high-speed X-ray imaging. Sci Rep 9:1–10. https://doi.org/10.1038/s41598-019-38862-7
54. Lecis N, Mariani M, Beltrami R et al (2021) Effects of process parameters, debinding and sintering on the microstructure of 316L stainless steel produced by binder jetting. Mater Sci Eng A 828:142108. https://doi.org/10.1016/j.msea.2021.142108
55. Z Chen W Chen L Chen et al 2022 Influence of initial relative densities on the sintering behavior and mechanical behavior of 316 L stainless steel fabricated by binder jet 3D printing Mater Today Commun 31 https://doi.org/10.1016/j.mtcomm.2022.103369
56. Lores A, Azumendi N, Agote I, Andres U (2020) A step towards a robust binder jetting technology: Process parameter optimization for 17-4 PH steel to increase powder bed homogeneity. In: Proceedings of the Euro PM2020 Virtual Congress, Online, pp 5–7
57. Azurmendi N, Lores A, Guraya C, Agote I (2020) Binder jetting of high dimensional stability alloy for space applications. Euro PM 2018 Congress and Exhibition 156875
58. Chen H, Zhao YF (2016) Process parameters optimization for improving surface quality and manufacturing accuracy of binder jetting additive manufacturing process. Rapid Prototyp J 22:527–538. https://doi.org/10.1108/RPJ-11-2014-0149
59. Jiang R, Monteil L, Kimes K et al (2021) Influence of powder type and binder saturation on binder jet 3D–printed and sintered Inconel 625 samples. Int J Adv Manuf Technol 116:3827–3838. https://doi.org/10.1007/s00170-021-07496-3
60. Zhao H, Ye C, Fan Z, Wang C (2017) 3D printing of CaO-based ceramic core using nanozirconia suspension as a binder. J Eur Ceram Soc 37:5119–5125. https://doi.org/10.1016/j.jeurceramsoc.2017.06.050
61. M Zago NFM Lecis M Vedani I Cristofolini 2022 Geometrical issues in design for binder jetting - the effect of anisotropic dimensional change on sintering Lect Notes Mech Eng 410–421 https://doi.org/10.1007/978-3-030-91234-5_42
62. Zago M, Lecis N, Mariani M, Cristofolini I (2022) Analysis of the flatness form error in binder jetting process as affected by the inclination angle. Metals-Basel 12(3):430. https://doi.org/10.3390/met12030430